science, engineering and health studies

Research Article

Science, Engineering and Health Studies
https://lio1.tci-thaijo.org/index.php/sehs
ISSN (Online): 2630-0087

Optimal screw configurations of broad and curved broad locking compression plates for femoral shaft fractures

Nakarin Jullapram[1] *and Nattapon Chantarapanich*[1,2*]

[1] Department of Mechanical Engineering, Faculty of Engineering at Sriracha, Kasetsart University, Chonburi 20230, Thailand
[2] Digital Industrial Design and Manufacturing Research Unit, Faculty of Engineering at Sriracha, Kasetsart University, Chonburi 20230, Thailand

***Corresponding author**: Nattapon Chantarapanich nattapon@eng.src.ku.ac.th*

***Received**: 14 June 2023*
***Revised**: 31 August 2023*
***Accepted**: 19 September 2023*
***Published**: 21 December 2023*

***Citation**: Jullapram, N., and Chantarapanich, N. (2023). Optimal screw configurations of broad and curved broad locking compression plates for femoral shaft fractures. Science, Engineering and Health Studies, 17, 23040008.*

ABSTRACT

The optimal configuration and number of screws used in a broad locking compression plate (B-LCP) and a curved broad locking compression plate (CB-LCP) to stabilize a femoral shaft fracture were determined using finite element (FE) analysis. A three-dimensional model of the femur and its transverse fracture at the mid-shaft region was created with widths of 10, 20 and 30 mm. The B-LCP and CB-LCP were attached to the femur model to retain the fracture using 3 to 5 screws placed equally and symmetrically for the proximal and distal segments. There were 16 screw fixation configurations for each B-LCP and CB-LCP, producing a total of 96 FE cases. The B-LCP screw configuration without secured screws at a position close to the fracture presented lower stress compared to the other configurations, while for CB-LCP, implant stress reduced when screws were secured close to the fracture. For both B-LCP and CB-LCP, elastic strain at the fracture site increased at greater working length. Bone stress using 6 screws in B-LCP was higher than when using 8 and 10 screws, with slight differences between bone stress values of 8 and 10 screws. Bone stresses in CB-LCP were in the same range, regardless of the number of screws. Three consecutive screws in CB-LCP at positions adjacent to the fracture produced lower bone stress than the other configurations. Fracture gap width had a slight influence on implant stress, elastic strain and bone stress. Results suggested that both LCPs should have four screws on each fragment, while screws on B-LCPs at positions close to the fracture without other adjacent screws should be avoided. Screws located close to the fracture gave best results for CB-LCP.

Keywords: broad locking compression plate; curved broad locking compression plate; screw configuration; femur; shaft fracture; finite element analysis

1. INTRODUCTION

Femoral shaft fractures result in deformed limbs that require correct anatomical alignment. Proper reduction procedures are necessary and the fragments must be aligned in close proximity to allow for bone healing at the fracture sites (Marsell and Einhorn, 2011). One method to do so is to use a locking compression plate (LCP) (Amornmoragot, 2019; Apivatthakakul et al., 2012). The two types of LCP include a broad LCP (B-LCP) and a curved broad LCP (CB-LCP). Both plates have various screw holes that provide surgeons with alternatives for inserting locking screws in different configurations depending on fracture type (Wagner, 2003). Different screw positions and configurations provide

diverse stiffness and strength of bone-implant constructs, while improper screw positions may increase the risk of clinical complications such as implant breakage (Bäcker et al., 2022; Dang et al., 2019; Lv et al., 2017; Tank et al., 2016; Marcomini et al., 2014; Kim et al., 2012) and fracture non-union. (Bäcker et al., 2022; Dang et al., 2019; Tank et al., 2016; Kim et al., 2012).

Both B-LCPs and CB-LCPs contain various screw holes providing many possible screw configurations. Poor choice of screw combinations may increase the risk of implant failure (Bucholz et al., 2010; Chen et al., 2010). Many studies have investigated screw configurations used for fracture fixation under different loading conditions (Rostamian et al., 2022; Sheng et al., 2019; Padron et al., 2017; Wittkowske et al., 2017; Lee et al., 2014), but case studies testing more than 3 screws on each fragment are limited (Sheng et al., 2019; Padron et al., 2017) based on the surgeon's experience (Wittkowske et al., 2017; Lee et al., 2014). Some studies (Rostamian et al., 2022; Lee et al., 2014) utilised optimisation algorithms in conjunction with finite element (FE) analysis to determine optimal screw configurations, but no attempts were made to minimise or maximize bone displacement as the primary objective. These studies (Rostamian et al., 2022; Sheng et al., 2019; Padron et al., 2017; Wittkowske et al., 2017; Lee et al., 2014) were also limited to B-LCP and did not consider CB-LCB. Therefore, the optimal screw configuration for both B-LCP and CB-LCB requires detailed investigation.

This study determined optimal screw configurations for both B-LCP and CB-LCP that provided sufficient strength and fracture stability with low risk of bone breakage for femoral shaft fractures. The FE method was used as a tool to assess all possible symmetrical screw configurations in proximal and distal femoral segments using at least 3 screws in each segment. Information obtained from this study will be beneficial for surgeons using LCPs to repair femoral diaphyseal fractures.

2. MATERIALS AND METHODS

2.1 Three-dimensional (3D) computer aided design model

Femur anatomy datum used for FE analysis in this study was obtained from a volunteer with no trauma record or bone deformity (Male, aged 24). The volunteer was scanned by a spiral computed tomography (CT) scanner (Philips Brilliance 64-slice, CT scanner, Philips, The Netherlands) with a 0.625 mm slice thickness and image resolution of 512x512 pixels. Peak output of the x-ray generator was 120 kV with tube current-time product of the x-ray at 260.61mAs. CT scan data were recorded as a stack of 2D cross sectional images in Digital Imaging and Communications in Medicine (DICOM) file format, which was then imported into the image processing software (3D Slicer software, slicer.org) (Fedorov et al., 2012) to reconstruct a 3D model of the femur. In the image processing software, Hounsfield unit (HU) values greater than 426 were applied as the threshold bone density range of the femur and used to produce a polygonal surface of the 3D femur model including the cortical surface and its intramedullary canal. Cancellous bone in the epiphysis corresponding to the 3D femur model was created based on the indicated cancellous layer appearing in the CT images. The cortical bone, cancellous bone and intramedullary canal models were then converted to 3D parametric Computer Aided Design (CAD) models in CAD software (VISI, Hexagon AB, Sweden). The fracture under consideration was a mid-shaft transverse fracture according to the AO/OTA as 32A3 (Meinberg et al., 2018). The fracture gap at mid-shaft was created with widths of 10, 20 and 30 mm that are commonly found as a result of accidents (Johnson and Urist, 2000).

Synthes 12-hole 4.5 mm B-LCP and Synthes 12-hole 4.5 mm CB-LCP were used in this study with 5.0 mm diameter locking screws. Dimensions of both plates and locking screws were obtained using a Dino-Lite digital microscope (Dino-Lite, AnMo Electronics Corporation, Taiwan) and used to create 3D models of implants using CAD software (VISI, Hexagon AB, Sweden). The screw model was omitted to simplify the FE analysis. The implant model was aligned to the intact femur in CAD software (VISI, Hexagon AB, Sweden) and the cortical bone was subtracted to the screws to complete the bone-implant construct, as shown in Figure 1.

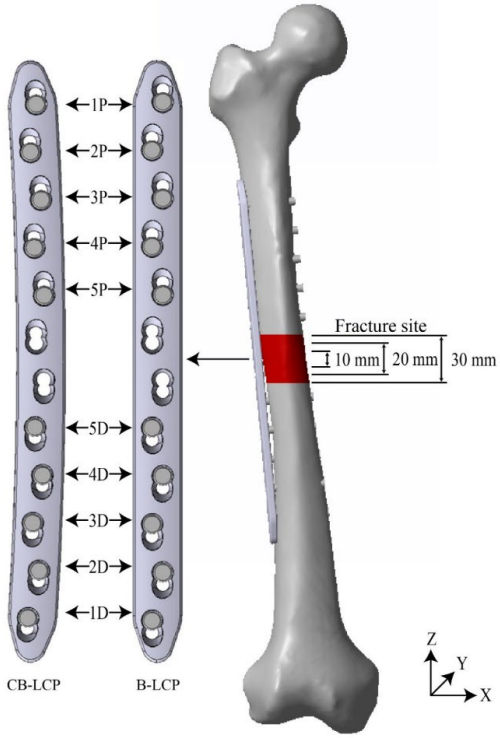

Figure 1. 3D femur-implant models with screw position designation
Note: x: lateral-medial, y: anterior-posterior, and z: distal-proximal

The study design included fractures stabilized by B-LCP and CB-LCP with at least three screws in each bone fragment (Lee et al., 2014). The femur fragments were fitted with a maximum of 5 screws, with 3–5 screw placements for each fragment. The number of screws was equal and symmetrical between proximal and distal fragments, giving 16 screw fixation configurations for B-LCP and CB-LCP, as shown in Figure 2. The three gap widths of the fractures produced 96 cases for analysis.

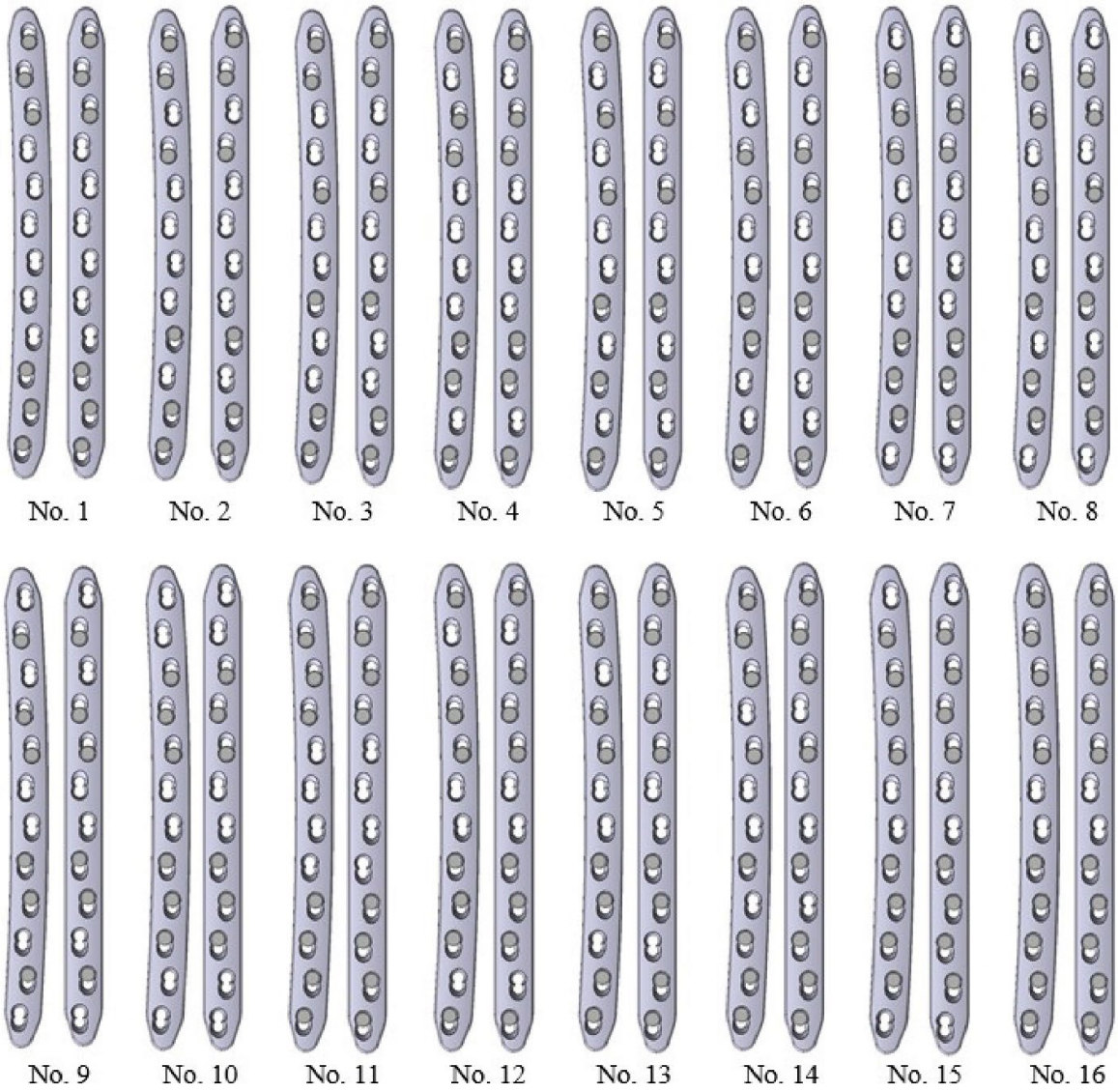

Figure 2. Screw configurations

2.2 Element generation

The FE models were built from four-node tetrahedral elements (Element type 134) using automatic mesh generation software (MSC Patran, MSC Software, Inc., USA) based on the 3D CAD model of the femur and implants. The element sizes near holes of implants and cortical bones were finer than in other regions. The optimal number of elements for each FE model was determined based on the convergence test results.

2.3 Material properties

Material properties were assumed to be homogenous and linearly elastic. The femur was set as anisotropic, whereas other regions were isotropic. The study was set during the acute phase of fracture because it is a critical healing phase without callus formation which bears the load from the implant. Therefore, the fracture site was defined as initial connective tissue. The plates and screw implants were made from a medical grade titanium alloy. Table 1 shows the relevant material properties used for the FE analyses (Chantarapanich et al., 2016; Krone and Schuster; 2006; Taylor et al., 2002).

Table 1. Material properties (Chantarapanich et al., 2016; Krone and Schuster, 2006; Taylor et al., 2002)

Material	Elastic modulus (MPa)	Poisson's ratio	Shear modulus (MPa)
Cortical bone	E_1=17,900 E_2=18,800 E_3=22,800	ν_{12}=0.26 ν_{23}=0.31 ν_{31}=0.38	G_{12}=5,710 G_{23}=7,110 G_{31}=6,580
Cancellous bone	E_1=676 E_2=968 E_3=1,352	ν_{12}=0.30 ν_{23}=0.30 ν_{31}=0.30	G_{12}=370 G_{23}=292 G_{31}=505
Initial connective tissue	E=3	v=0.40	
Titanium	E=110,000	v=0.33	

2.4 Boundary and contact conditions

The boundary conditions included physiological loads (i.e. body weight and muscle forces) and joint constraints. Physiological loads at 25% of gait cycles were used as this presented the maximum magnitude during walking (Behrens et al., 2009). Partial weight bearings were applied

for post-operative conditions as 51% of the body weight (Koval et al., 1998). Joint constraints were set according to previous literature (Behrens et al., 2009; Speirs et al., 2007). At the distal femoral condyle, intercondylar notch areas were fully constrained and both condylar compartments were set as floating bearings. At the hip joint, the femoral head was constrained in any transverse direction. Table 2 shows the magnitudes of physiological loads used in the FE analysis (Chantarapanich et al., 2016; Behrens et al., 2009), while Figure 3 shows FE models with boundary conditions.

All models used in the FE analysis were deformable. All bone regions were fully intact with each other without relative displacement. Bone and plate interfaces were allowed relative sliding with a friction coefficient of 0.30 (Jitprapaikulsarn et al., 2021). The locking screws were omitted to simplify the calculation. The portions of the locking screws anchored into cortical bone and parts of the screws secured into holes in the LCPs were also assumed to have no relative displacement between these interfaces.

Table 2. Physiological forces for FE analysis (Chantarapanich et al., 2016; Behrens et al., 2009)

Force	Magnitude (N)			Acting point
	x	y	z	
Hip contact	-230.2	115.1	-921.1	P1
Abductor	468	0	694	P2
Tensor fascia latae	-117	158.8	-75.2	P2
Vastus lateralis	-8.4	-108	-543	P3
Vastus medialis	-8.4	-33.4	-167	P4

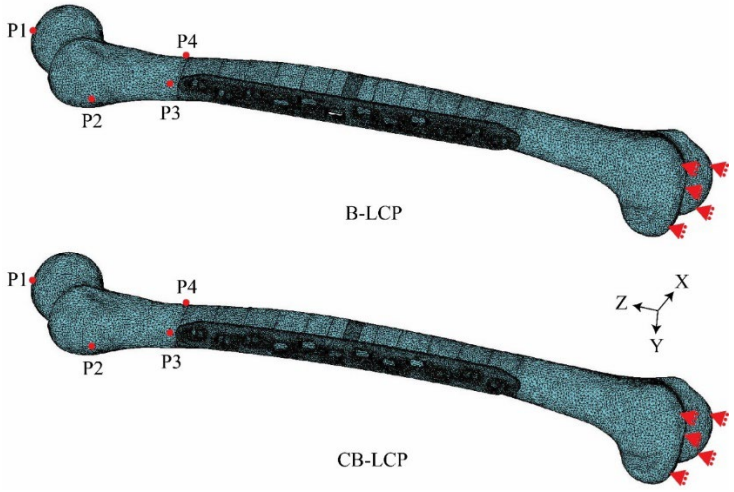

Figure 3. Boundary condition of FE model
Note: x: lateral-medial, y: anterior-posterior, and z: distal-proximal

2.5 Convergence test

The B-LCP and CB-LCP FE models with screw configuration No. 1 were selected for convergence testing. Five different numbers of elements were generated. To simulate an optimal number of elements, the FE model was assigned material properties, boundary conditions and contact conditions according to the descriptions in previous sections. The equivalent von Mises (EQV) stress on the implant was used as a monitored parameter to observe the convergence trend.

2.6 Mechanical test for FE model validation

Screw fixation configuration No. 4 was selected for mechanical testing of FE model validation. Proximal and distal segments of the femur were 3D-printed (3DP) from polylactic acid (PLA) filament (Verbatim, Mitsubishi Kagaku Media Co., Ltd., Japan) using the CR-10S fused deposition modeling (FDM) technique (Shenzhen Creality 3D Technology Co., Ltd., PR China).

Printing parameters included a 0.2 mm layer thickness, 210 °C nozzle temperature, 60 °C platform temperature, 30 mm/s printing speed, 45° cross-hatch raster angle and a rectilinear infilled pattern. Using this setting, the 3DP femur segments had mechanical properties according to the study of Chaitat et al. (2022).

The B-LCP was placed on the lateral side of the 3DP femur, with the position conforming to that set in the FE model. The B-LCP was then secured with 3 locking screws on each segment before the distal end of the femur was mounted in resin. Four strain gauges (Strain gauge model: KFP-2-120-C1-65L1M2R, Kyowa Electronic Instruments Co., Ltd., Japan) were attached on the anterior side of the 3DP femur with a bonding agent (Strain gauge instantaneous adhesive model: CC-33A, Kyowa Electronic Instruments Co., Ltd., Japan). Lead wires from each strain gauge were connected to the data logger (Quarter bridge system, Strain measuring unit model: EDX-10B and EDX-11A, Kyowa Electronic Instruments Co., Ltd., Japan). Data signals were sent through a universal serial bus (USB) cable connected between the data logger and the personal computer to display numeric strain values.

The construct of the fractured 3DP femur fixed with B-LCP was applied to a 750 N vertical compressive load at the femoral head using a universal testing machine (UTM) (UH-1000, Shimadzu Crop, Japan). Mechanical test equipment settings are shown in Figure 4. The obtained strain value was then compared with the FE strain result using the same model and conditions.

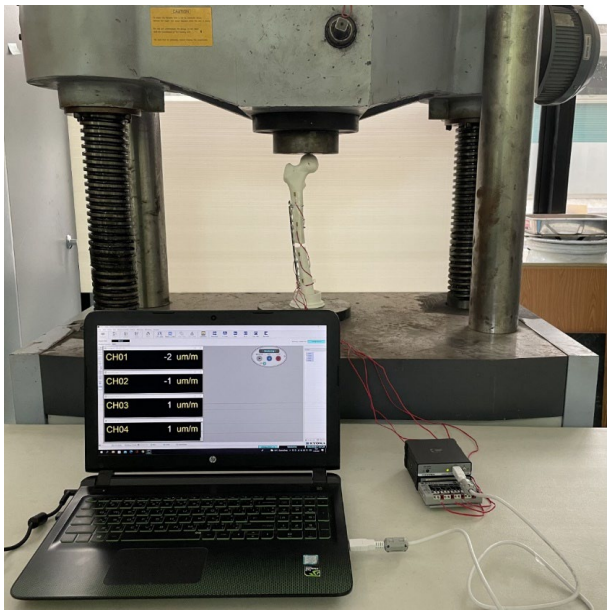

Figure 4. Equipment setting for mechanical test

3. RESULTS

3.1 Element convergence test

The element convergence test results are shown in Figure 5. Maximum EQV stress of B-LCP and CB-LCP differed by less than 4.0% (Jitprapaikulsarn et al., 2021; Chen et al., 2010) when the number of elements exceeded 797,634 (186,246 nodes) for the CB-LCP FE models and 799,454 elements (187,572 nodes) for the B-LCP FE models. Therefore, the number of elements used for FE analysis was selected according to these numbers.

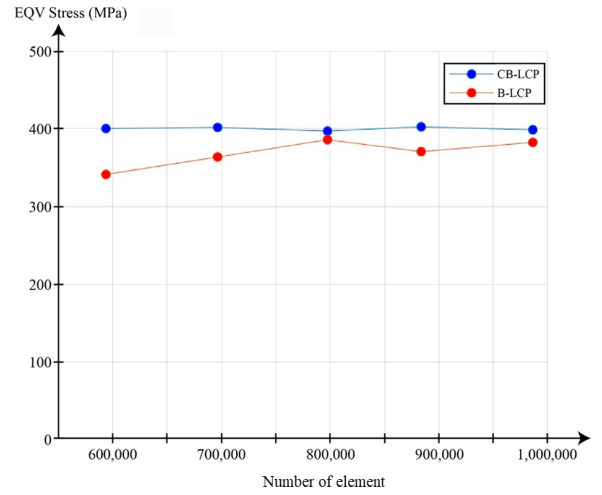

Figure 5. Convergence test result

3.2 Mechanical validation

The magnitude trend measured by strain gauges during the mechanical test conformed to results obtained from the FE analysis, as shown in Figure 6. Maximum strain was found at position No. 4 (distal segment), whereas minimum strain was found at position No. 3 (below the fracture site). The largest difference between values from the mechanical test and FE analysis was 3.2%, occurring at position No. 3 (below the fracture site). These values did not exceed the acceptable limit (Chantarapanich et al., 2017; Sivarao et al., 2015); therefore, the FE model with boundary and contact conditions described in this study was considered reliable.

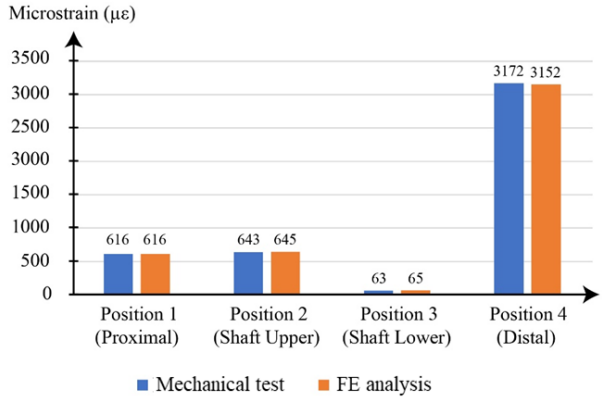

Figure 6. Comparison between mechanical test and FE analysis results.

3.3 EQV stress of B-LCP and CB-LCP

The EQV stress was used to assess the risk of implant failure when retaining the fracture. Under physiological loads, concentrations of EQV stress exhibited on B-LCP and CB-LCP were observed in the regions above and below the fracture site to the first locking holes, with screws secured as shown in Figures 7–12. Numerical results of implant EQV stress on the B-LCP and CB-LCP are shown in Figures S1–S3. Fracture gap width affected EQV stress on B-LCP and CB-LCP with a wider gap giving greater EQV stress in most cases, except for B-LCP with (1) screw No.4P/No.4D without screw No.3P/No.3D (screw configuration Nos. 2, 6, 9 and 13) and (2) screw No.5P/No.5D without screw No.4P/No.4D (screw configuration Nos. 5, 8 and 14) used to fix the fracture, where EQV stress was lower at a wider gap width.

CB-LCP configurations having 6, 8 and 10 screws secured at position No.5P/No.5D demonstrated lower EQV stress compared to the other configurations. The EQV stress of configurations falling within this criterion ranged 224.3–277.1 MPa for 10 mm gap width, 238.0–286.6 MPa for 20 mm gap width, and 239.8–290.2 MPa for 30 mm gap width. The other configurations ranged 298.1–397.1 MPa for 10 mm gap width, 325.3–383.9 MPa for 20 mm gap width, and 335.7–382.2 MPa for 30 mm gap width.

For B-LCP, any configuration without a secured screw at position No.5P/No.5D presented lower EQV stress than the other configurations. The EQV stress of configurations falling within this criterion ranged 218.4–385.9 MPa for 10 mm gap width, 227.2–422.1 MPa for 20 mm gap width, and 286.5–454.1 MPa for 30 mm gap width. The other configurations with a secured screw at position No.5P/No.5D ranged 282.6–525.4 MPa for 10 mm gap width, 340.1–536.8 MPa for 20 mm gap width, and 308.2–566.1 MPa for 30 mm gap width.

3.4 Fracture stability

Elastic strain at the fracture site indicated fracture stability. Figures S4–S6 report the elastic strain at the

fracture site after stabilizing with B-LCP and CB-LCP using different screw configurations. The stability depended on the distance of the first screw position from the fracture site, regardless of plate type (CB-LCP or B-LCP) or number of screws. Screw configuration with the first screw position from the fracture site at No.5P/No.5D demonstrated lower elastic strain, i.e. better stability, relative to the first screw position away from the fracture site at No.4P/No.4D and No.3P/No. 3D, as summarized in Table 3.

3.5 Bone stress

Highest bone stress was concentrated at the last bone hole of the femur fragment (proximal or distal fragment), as shown in Figures 13–18. Numerical bone stress results are shown in Figures S7–S9. For B-LCP, bone stress using 6 screws had a higher value than using 8 and 10 screws, while bone stress using 8 and 10 screws was slightly different. By contrast, bone stress values using CB-LCP were similar, regardless of the number of screws used. However, three consecutive screws in CB-LCP at positions adjacent to the fracture produced lower bone stress than the other screw configurations for each gap width (84.6–88.3 MPa for 10 mm gap width, 85.5–91.6 for 20 mm gap width, and 85.9–91.9 MPa for 30 mm gap width). Ranges of bone stress values are summarized in Table 4.

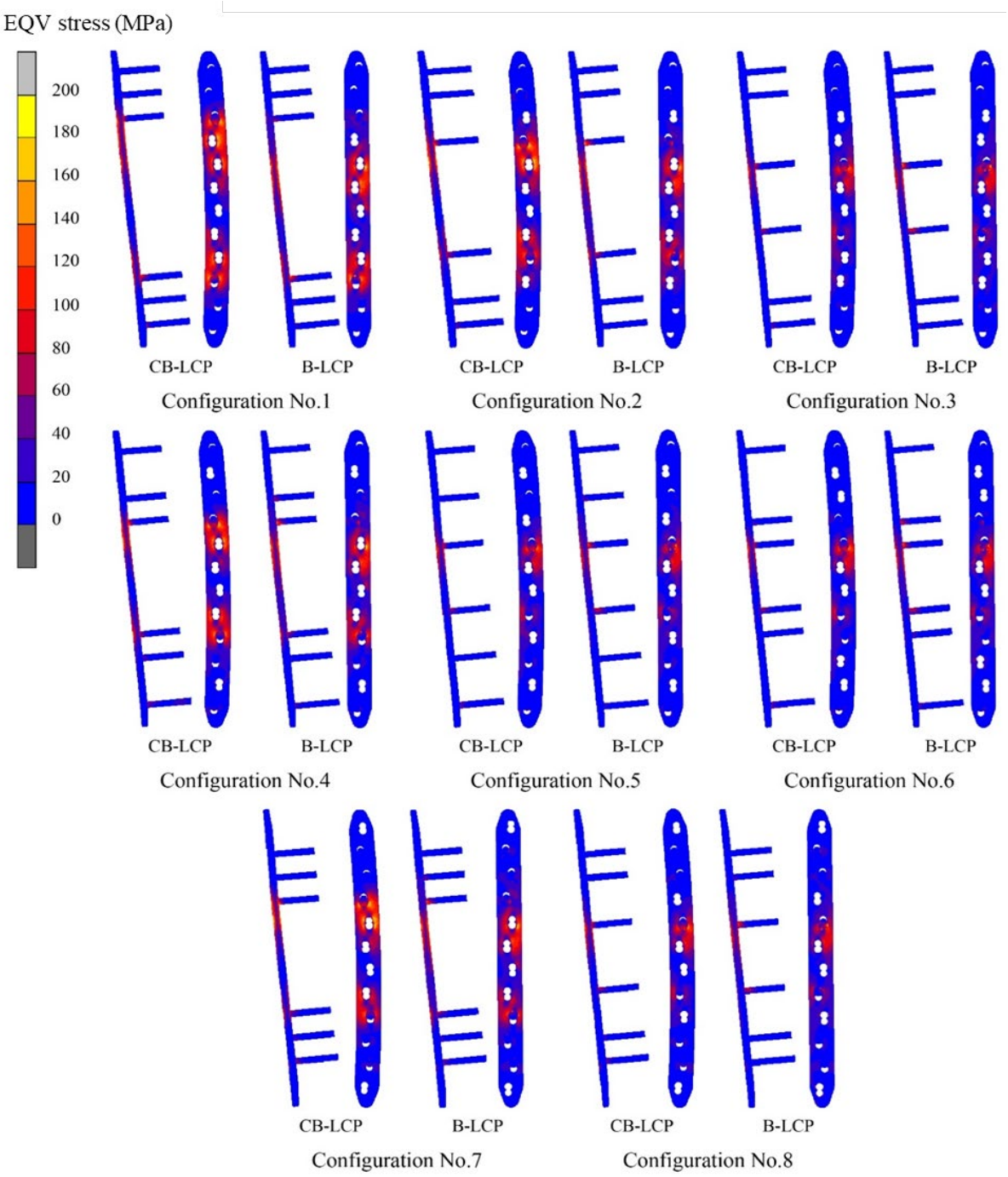

Figure 7. Implant stress distribution on B-LCP and CB-LCP for fracture gap width 10 mm: screw configuration No.1–No.8

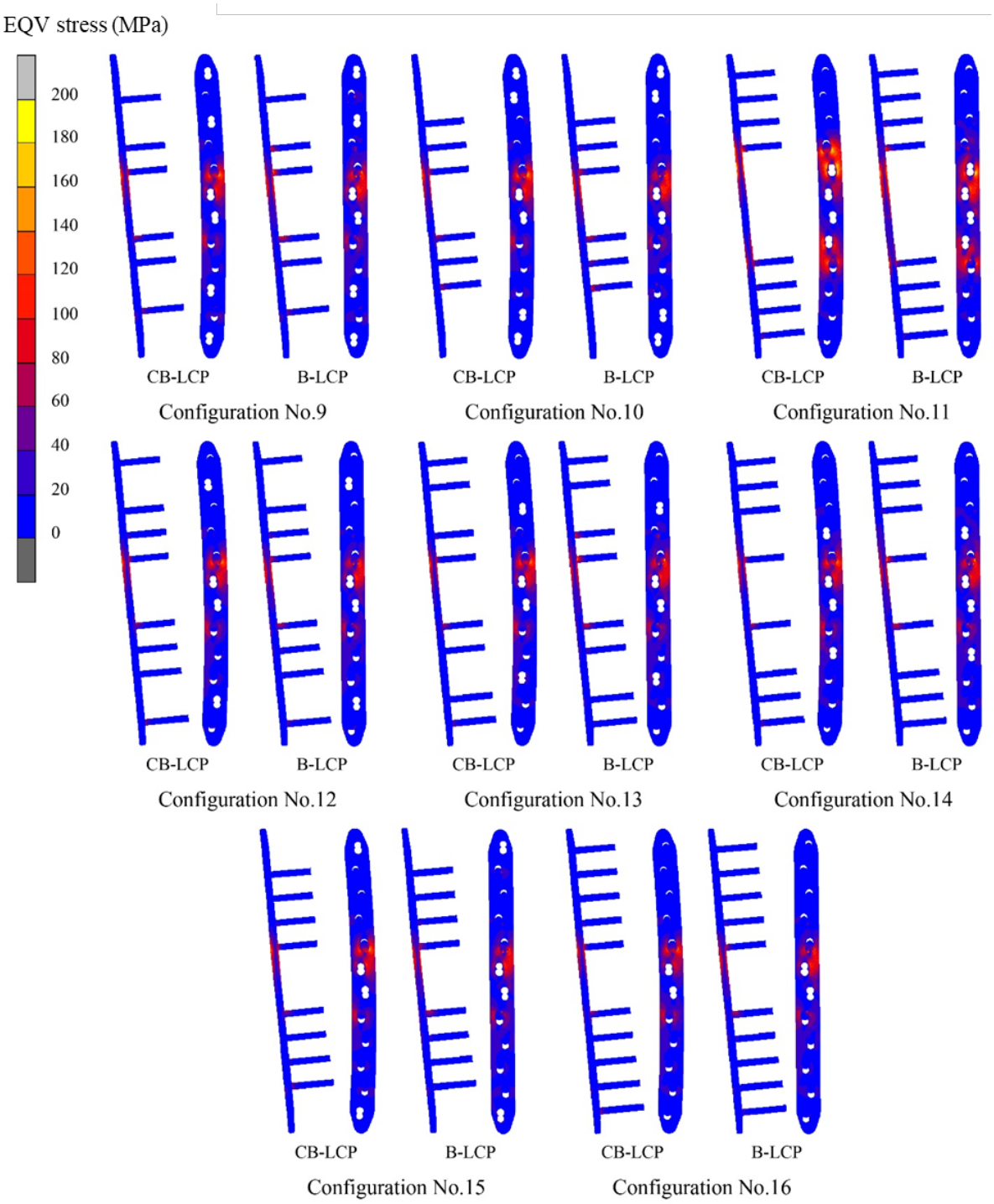

Figure 8. Implant stress distribution on B-LCP and CB-LCP for fracture gap width 10 mm: screw configuration No.9–No.16

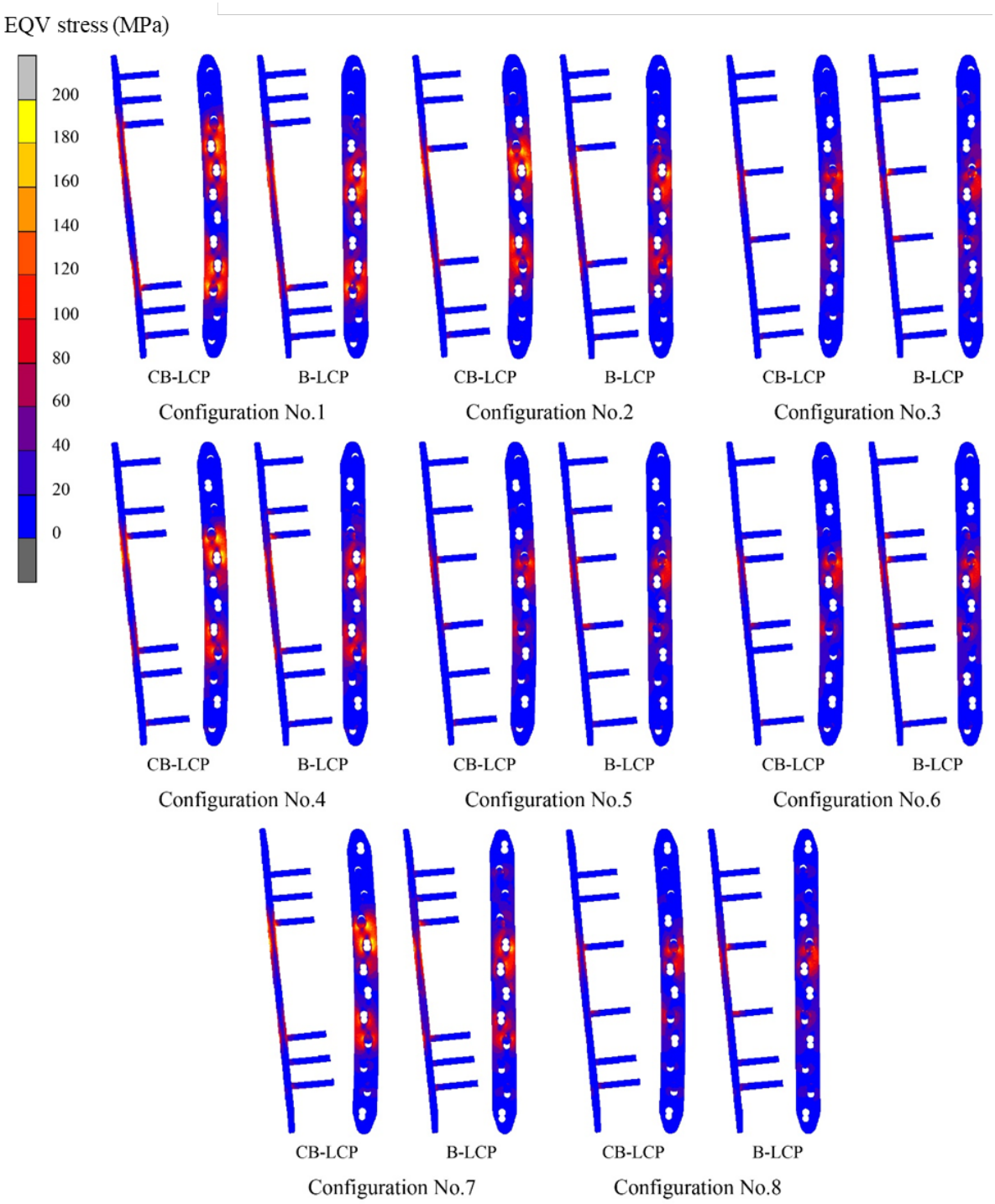

Figure 9. Implant stress distribution on B-LCP and CB-LCP for fracture gap width 20 mm: screw configuration No.1–No.8

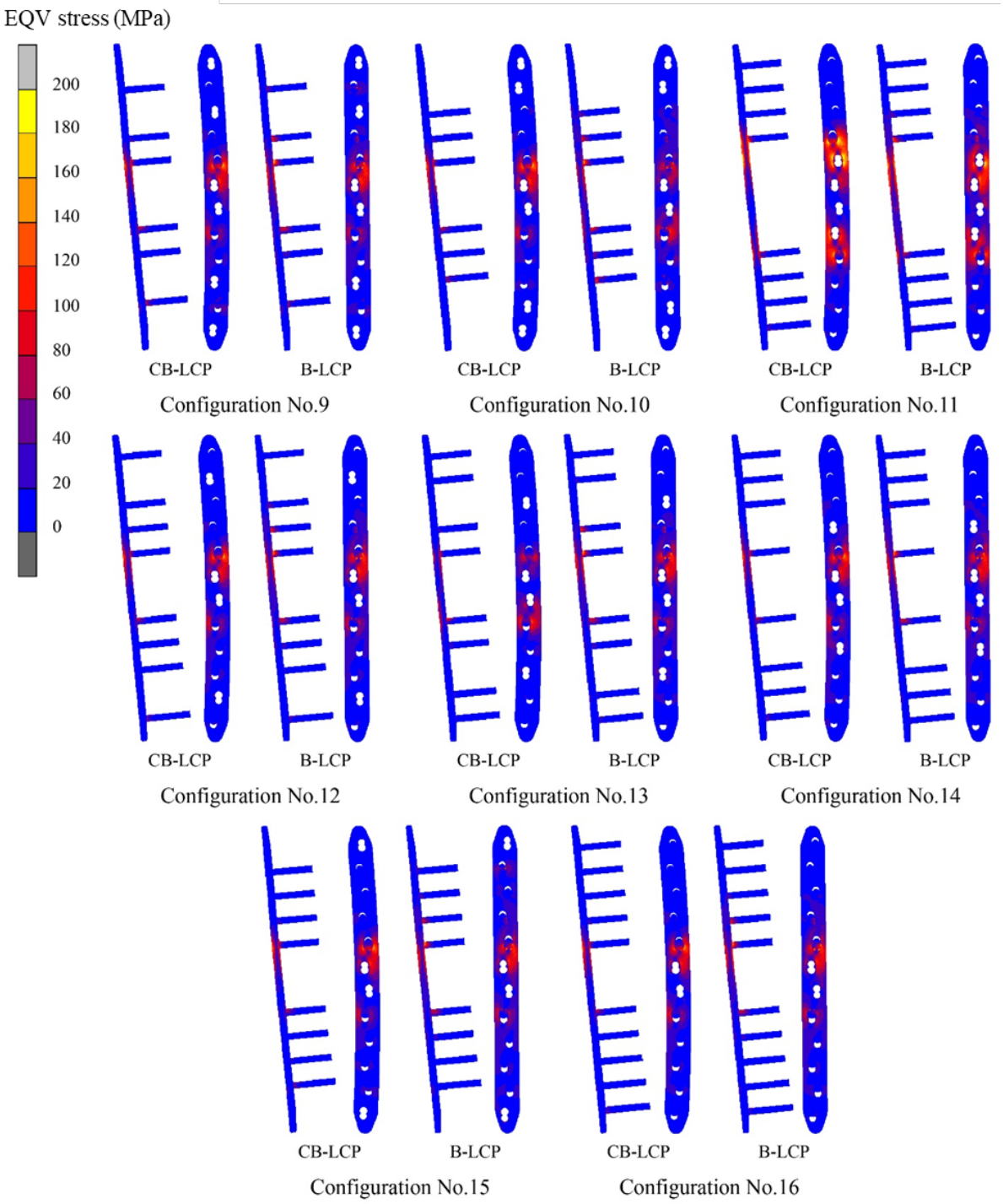

Figure 10. Implant stress distribution on B-LCP and CB-LCP for fracture gap width 20 mm: screw configuration No.9–No.16

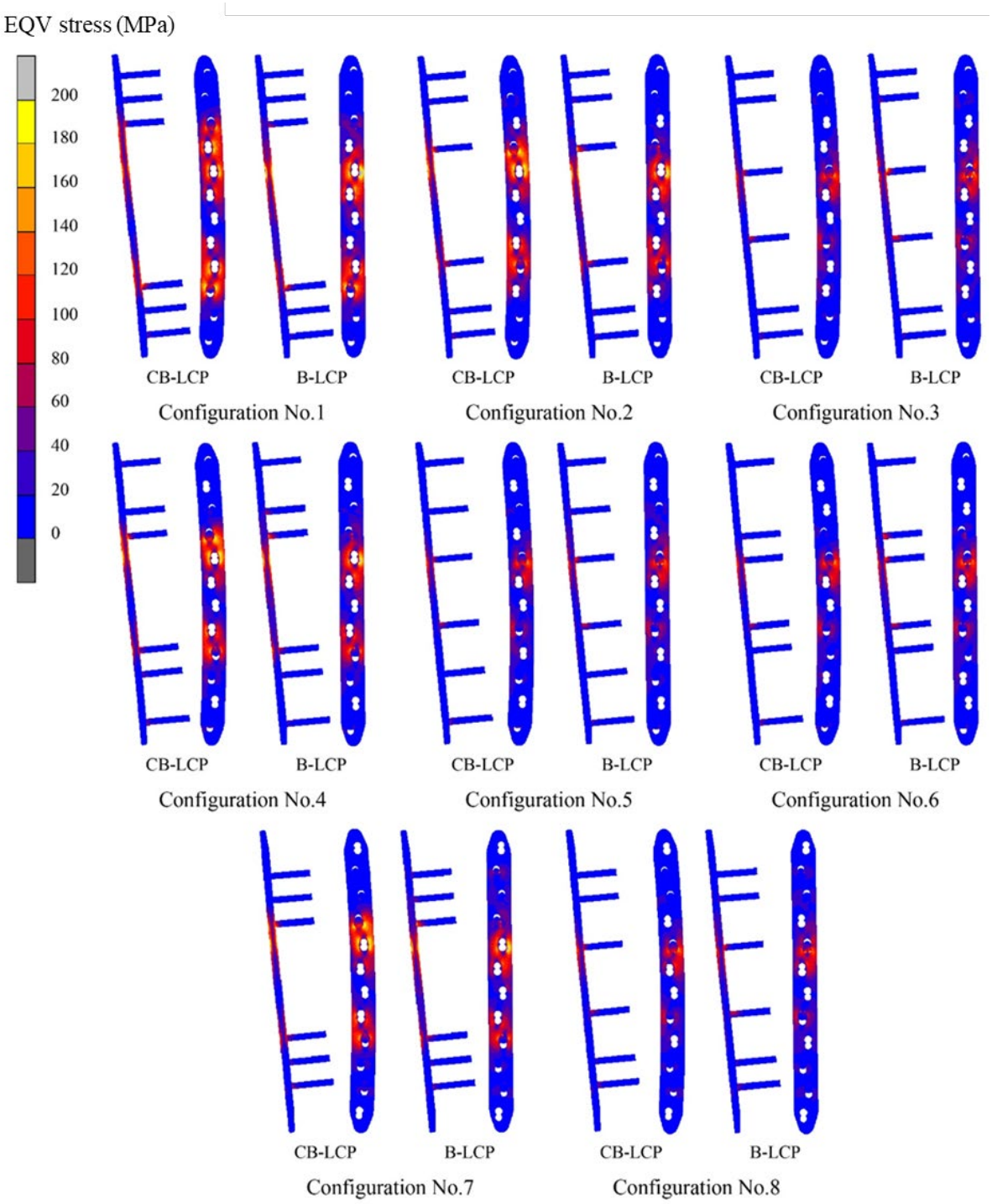

Figure 11. Implant stress distribution on B-LCP and CB-LCP for fracture gap width 30 mm: screw configuration No.1–No.8

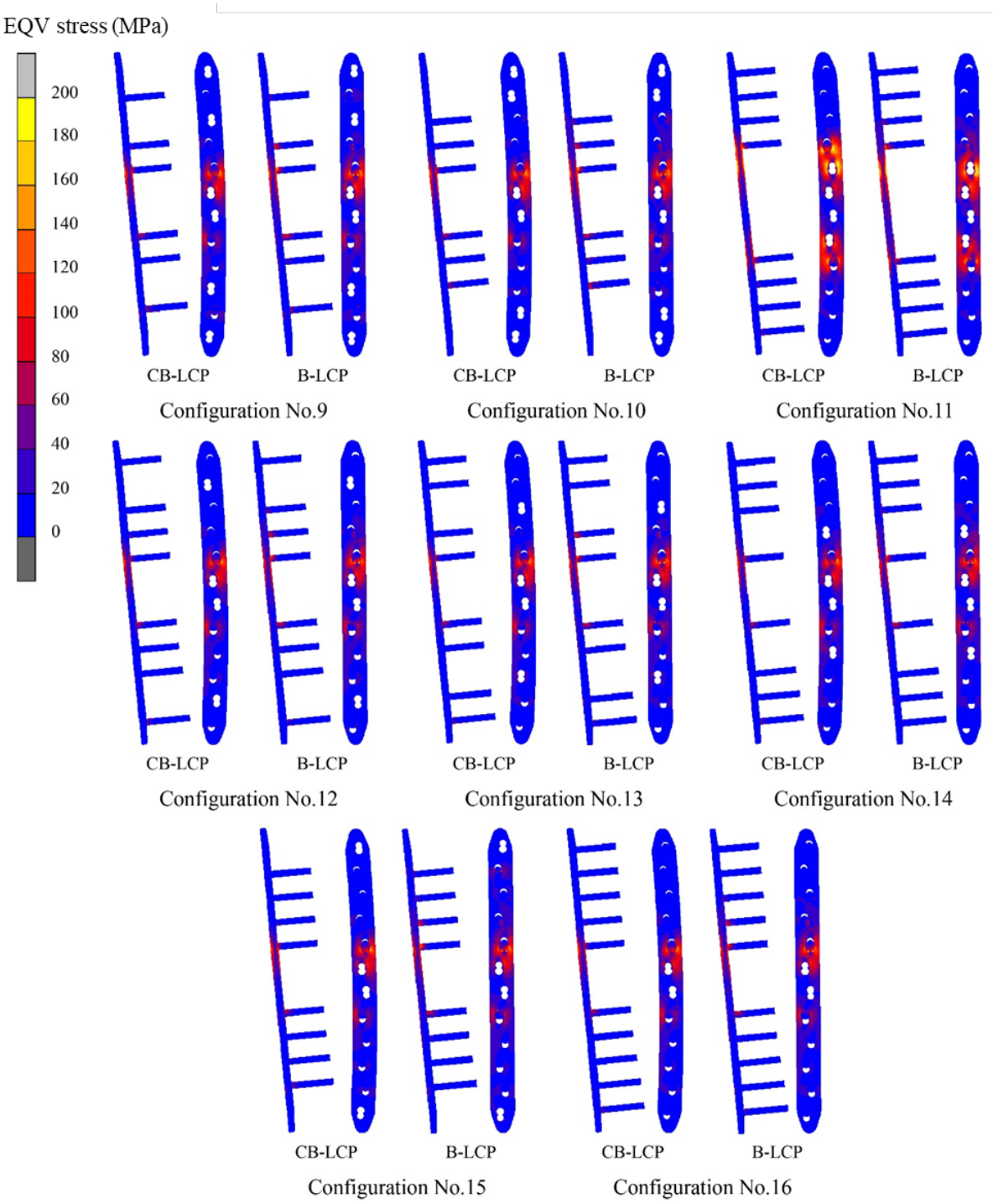

Figure 12. Implant stress distribution on B-LCP and CB-LCP for fracture gap width 30 mm: screw configuration No.9–No.16

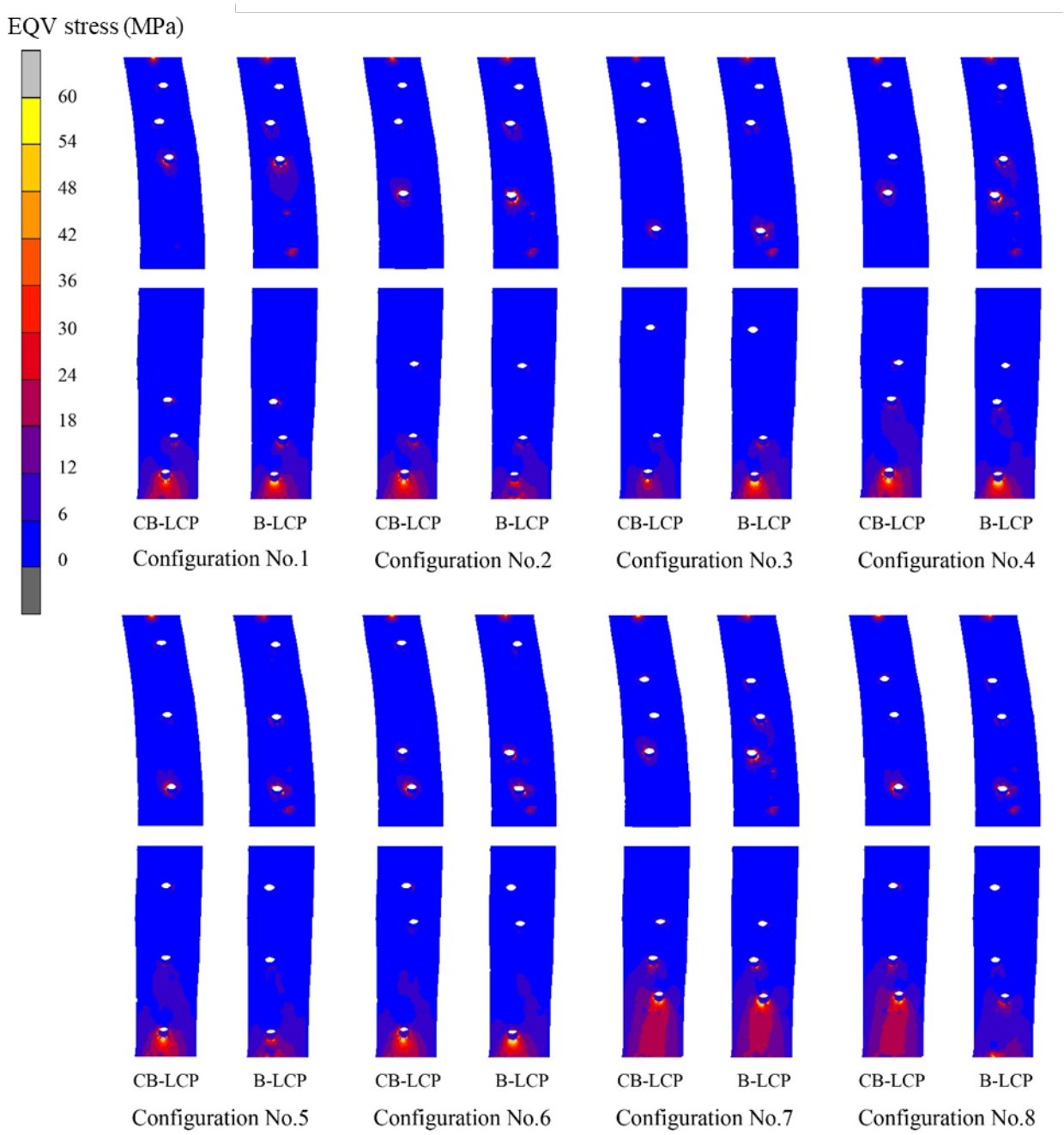

Figure 13. Bone stress distribution when retained with B-LCP and CB-LCP for fracture gap width 10 mm: screw configuration No.1–No.8

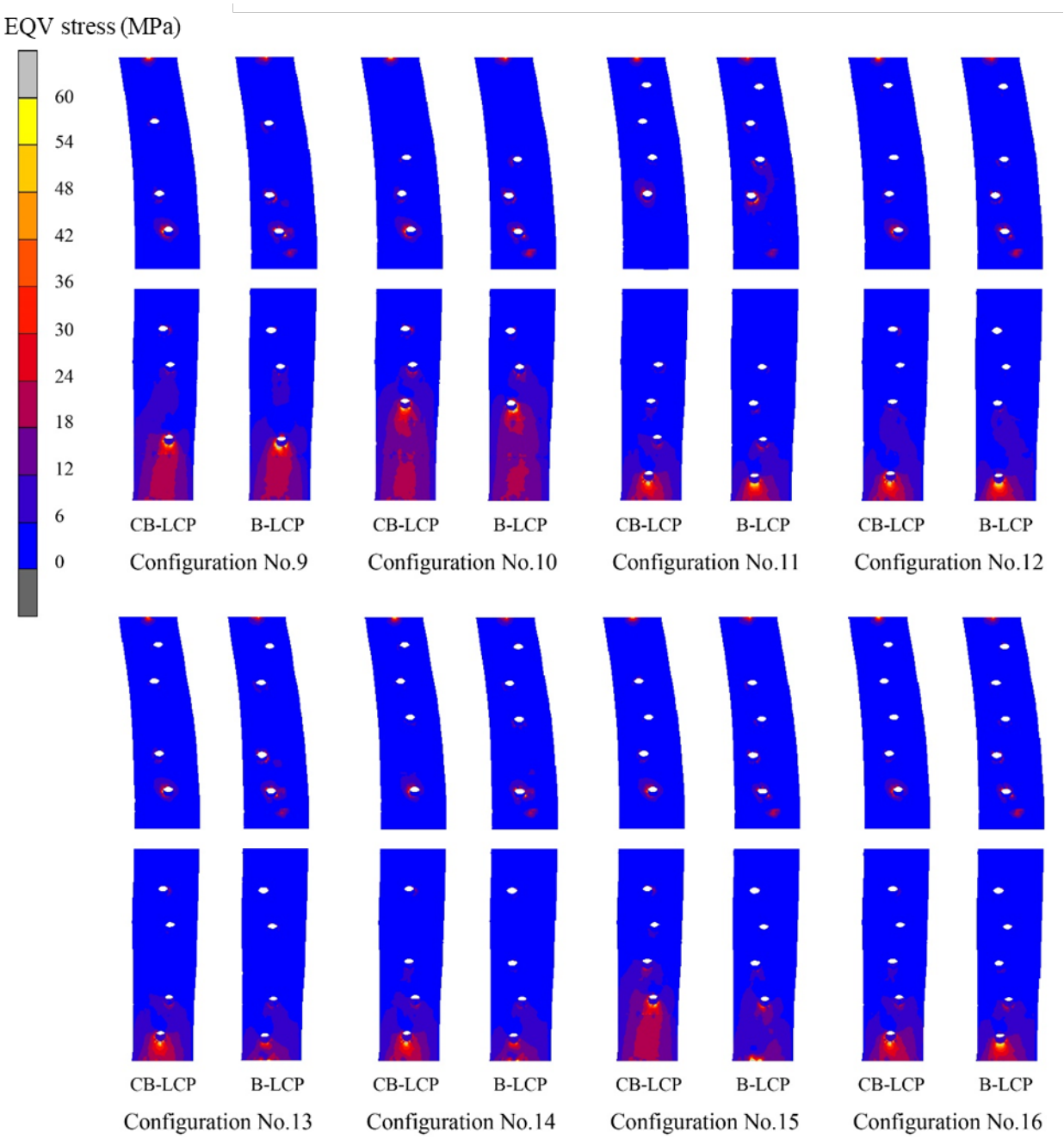

Figure 14. Bone stress distribution when retained with B-LCP and CB-LCP for fracture gap width 10 mm: screw configuration No.9–No.16

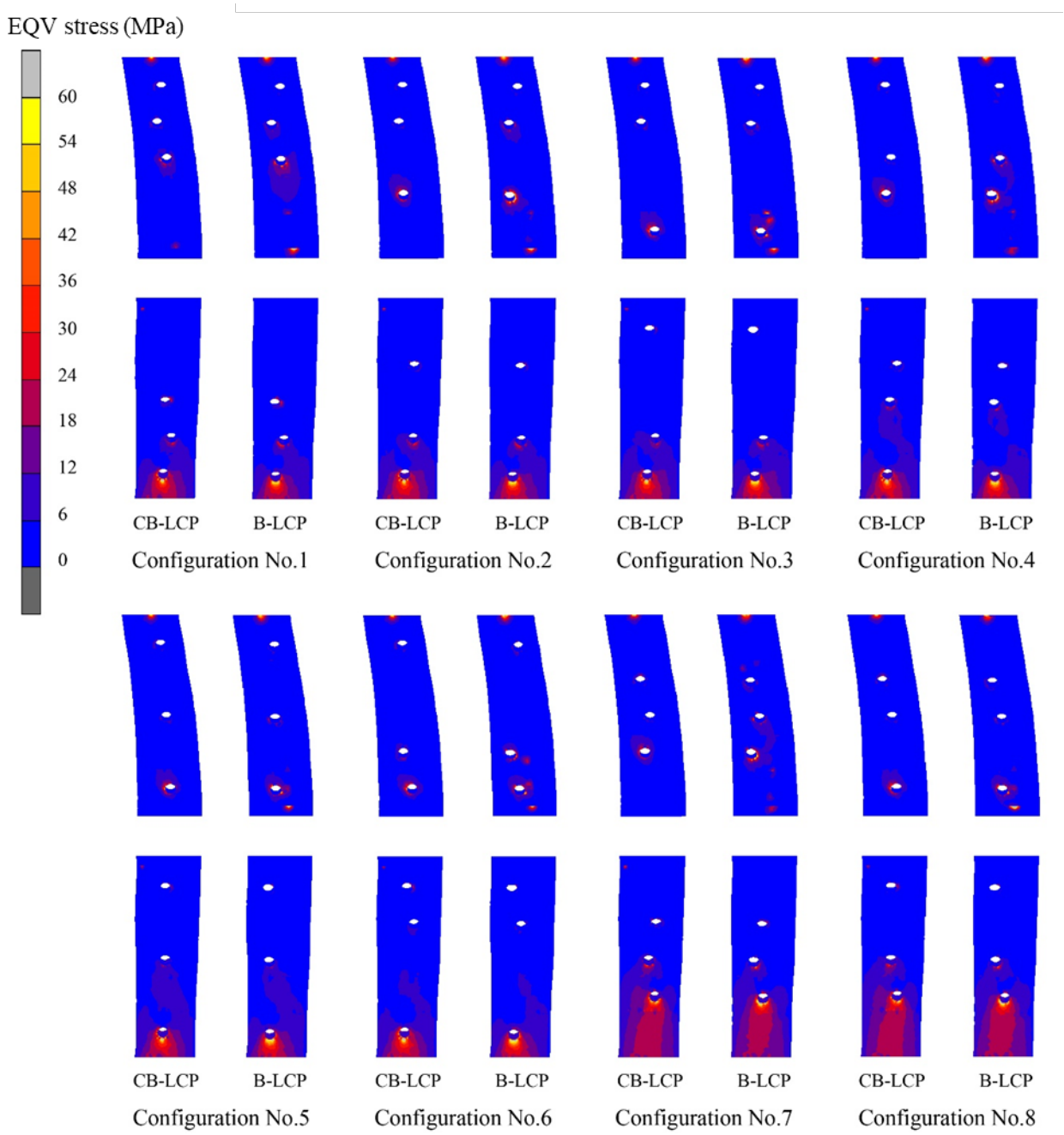

Figure 15. Bone stress distribution when retained with B-LCP and CB-LCP for fracture gap width 20 mm: screw configuration No.1–No.8

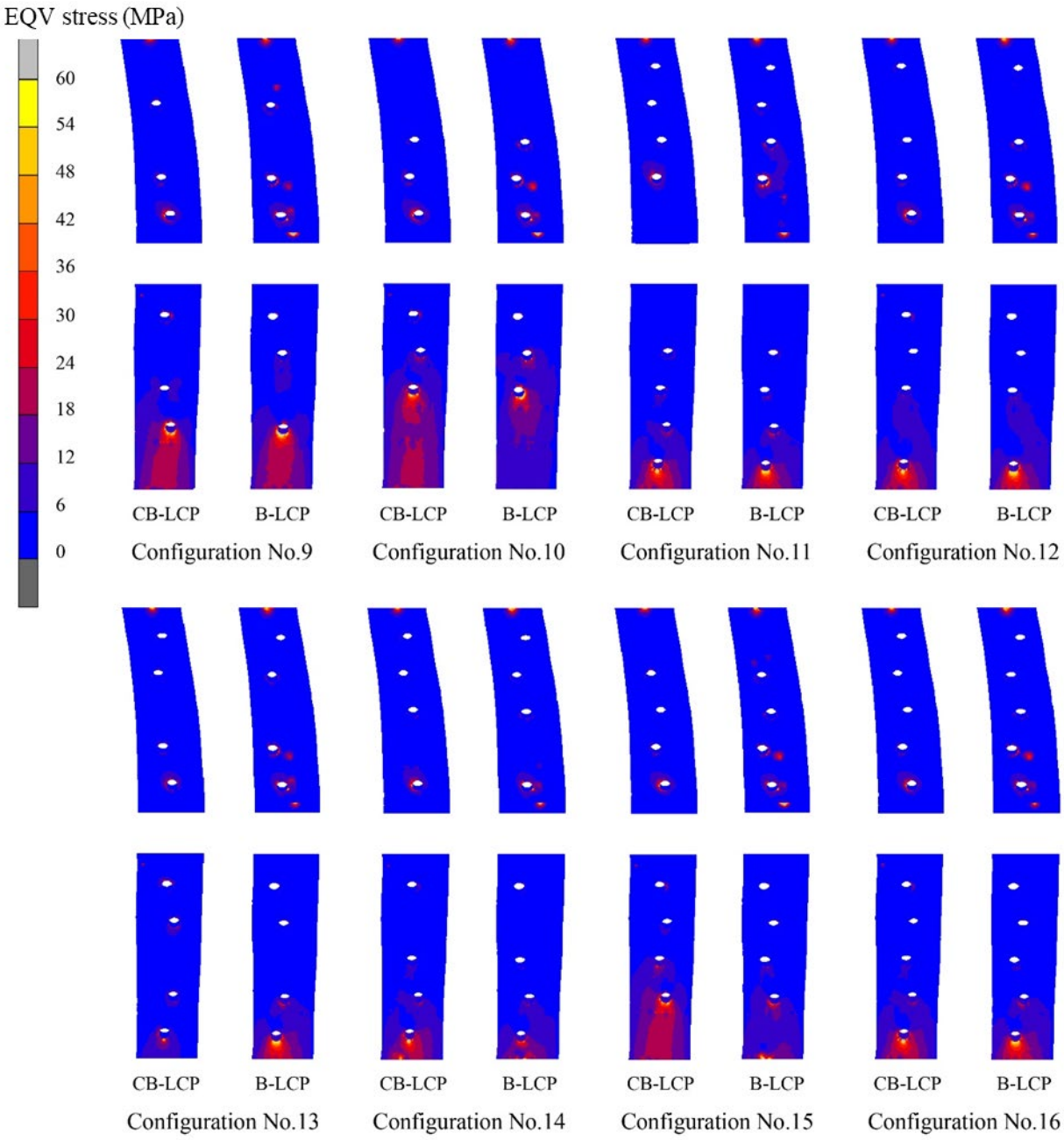

Figure 16. Bone stress distribution when retained with B-LCP and CB-LCP for fracture gap width 20 mm: screw configuration No.9–No.16

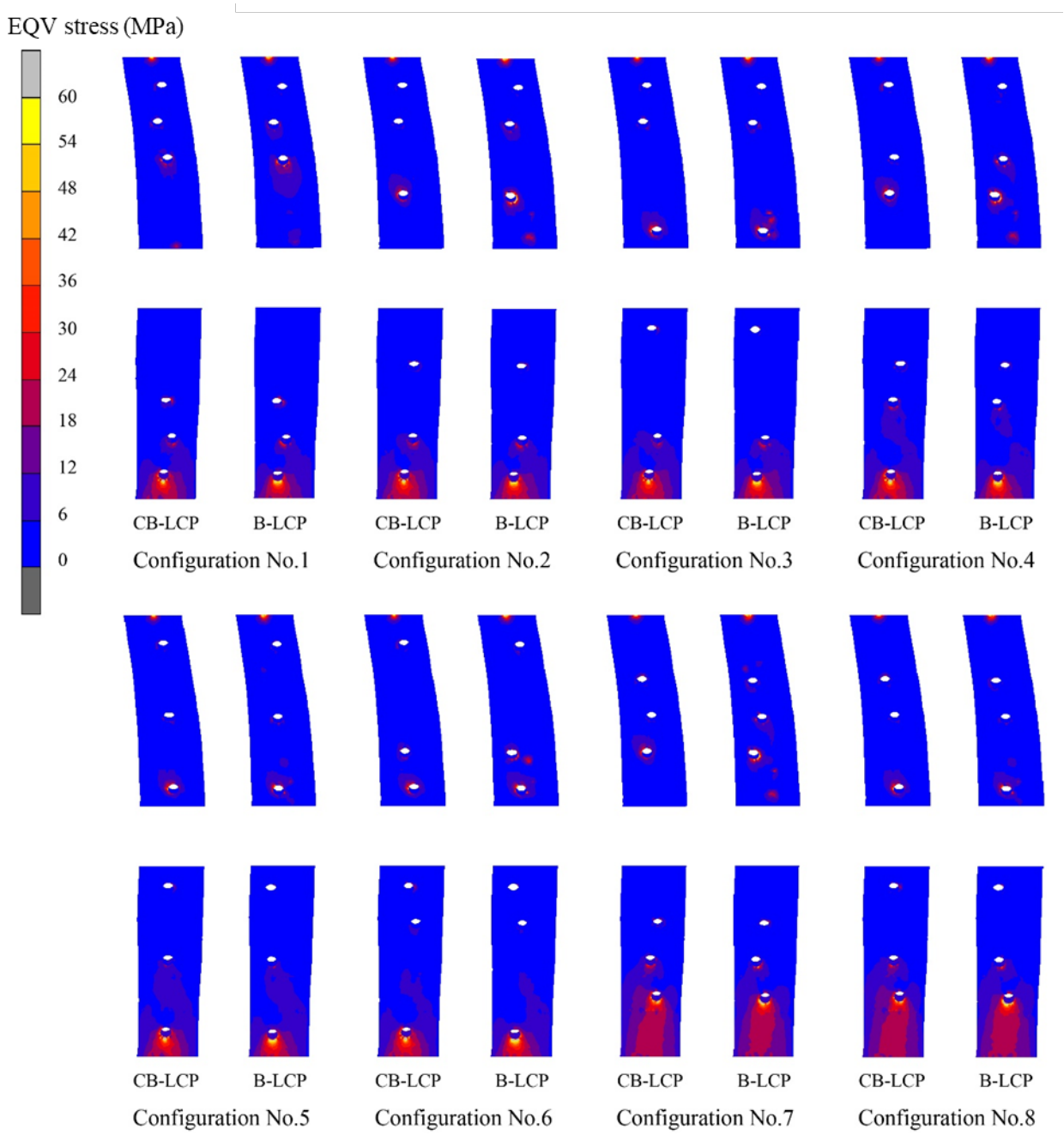

Figure 17. Bone stress distribution when retained with B-LCP and CB-LCP for fracture gap width 30 mm: screw configuration No.1–No.8

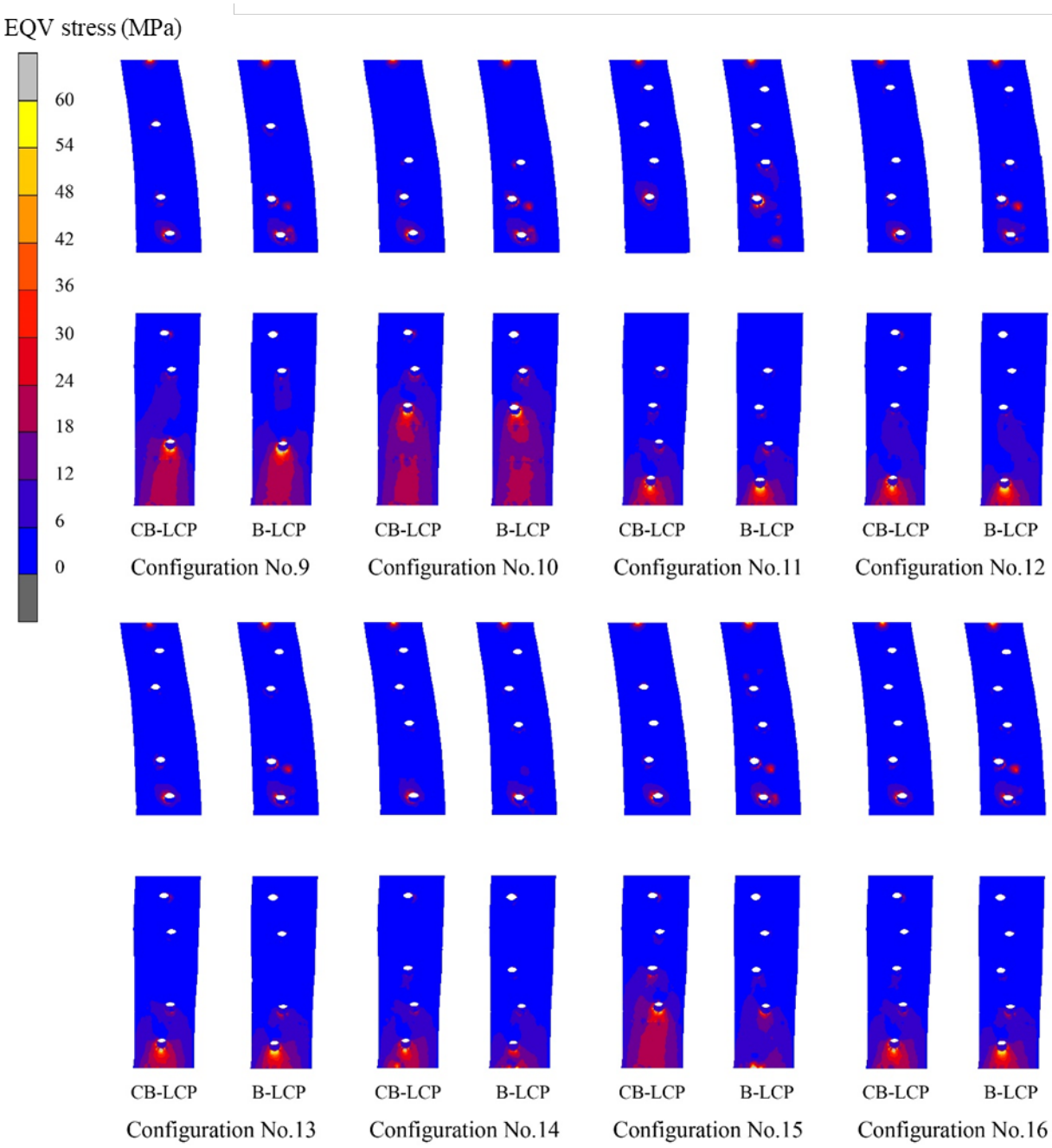

Figure 18. Bone stress distribution when retained with B-LCP and CB-LCP for fracture gap width 30 mm: screw configuration No.9–No.16

Table 3. Summary for range of elastic strain at the fracture site

Existence of the first screw position from fracture site	Fracture gap width (mm)	Strain at fracture site (με)	
		Retained with CB-LCP	Retained with B-LCP
No.5P/No.5D	10	80.6–112.1	97.4–109.9
	20	29.2–60.4	42.3–63.7
	30	26.6–33.4	26.0–29.1
No.4P/No.4D	10	186.1–213.2	133.9–139.5
	20	127.6–133.8	84.7–87.3
	30	75.2–84.4	52.3–53.8
No.3P/No.3D*	10	333.6	186.5
	20	208.1	124.2
	30	132.9	77.3

Note: *only screw configuration no.1 has 3p and 3d position as its first screw positions from the fracture.

Table 4. Summary for range of bone stress

Number of screws	Fracture gap width (mm)	Bone stress (MPa)	
		Retained with CB-LCP	Retained with B-LCP
Configuration with 6 screws	10	85.7–123.2	62.1–130.8
	20	87.0–103.6	75.0–128.0
	30	87.3–104.0	76.1–130.1
Configuration with 8 screws	10	84.6–98.4	52.2–86.9
	20	85.5–99.3	67.5–86.3
	30	85.9–99.8	63.2–87.4
Configuration with 10 screws*	10	88.3	79.1
	20	91.6	78.7
	30	91.9	79.7

Note: *Configuration with 10 screws had only one test.

4. DISCUSSION

This study determined the optimal screw configuration for B-LCP and CB-LCP to stabilize femoral shaft fractures. The FE method was utilized as a computational tool to compare biomechanical performances among various configurations of bone-implant constructs without performing costly physical mechanical tests (Rostamian et al., 2022; Sheng et al., 2019; Wittkowske et al., 2017; Lee et al., 2014). Loads used for FE analysis, including body weight and muscle forces, have been widely utilized to assess biomechanical performance for various femur fracture fixations such as cephalomedullary nail (Chantarapanich and Riansuwan, 2022), dynamic hip screw (DHS) (Jitprapaikulsarn et al., 2021) and LCP (Lee et al., 2014). Mechanical validation results showed that the developed FE model was reliable, with the maximum difference between FE results and mechanical tests based on similar settings at only 3.2%.

Hip contact loads acting at the proximal femur cause bending at the fracture site due to constraints at the distal femur with fracture at the middle of the femoral shaft. As a result, high EQV stress regions were observed on B-LCP/CB-LCP above and below the fracture site towards the first locking holes with secured screws. High bone stress occurred at the last bone hole of the proximal and distal fragments. It depended on location, the least distance between the last bone hole and posterior of cortical bone surface, which deformed under physiological loads.

An Asian femur has more curvature than a Caucasian femur (Thiesen et al., 2018). The B-LCP when attached to the lateral femur would position screws No.5P/No. 5D and No.4P/No.4D at the mid-anteroposterior of the femoral shaft, whereas the other screw positions were shifted to the anterior. The chances that load from a proximal femur concentrated on these screw positions were higher than others. Therefore, the B-LCP with secured screws at positions No.5P/No.5D and/or No.4P/No.4D with at least one adjacent empty screw hole demonstrated greater EQV stress magnitude compared to the other configurations, which could lead to implant failure. This finding corresponded to clinical reports by Bäcker et al. (2022), Lv et al. (2017), Marcomini et al. (2014) and Kim et al. (2012) who observed breaking of B-LCP around the fracture site when using screw positions close to the fracture. Screw positions far away from the fracture (long working length) produced higher EQV stress compared to closer positions (short working length), with effective working length from the fracture site to loading transfer point of the closest locking screw. Longer working length resulted in greater distance from the loading screw, producing higher bending stress.

In contrast to B-LCP, the curvature of CB-LCP conformed to the femoral curvature. All screw positions aligned well to the mid-anteroposterior of the femoral shaft. The screws shared equal loading functions. The distance of the screw positions affected the EQV stress magnitude in the same way as for B-LCP. Screw fixation close to the metaphyes without a secured screw close to the fracture site (position No.5P/No.5D) gave greater EQV stresses on implants than the other configurations, with possible breakage of CB-LCP around the fracture site. This observation from the FE results corresponded to clinical reports of Dang et al. (2019) and Tank et al. (2016) who reported that fixed screws a long distance apart caused breakage of the plate at the fracture site.

Better fracture stability for both B-LCP and CB-LCB was achieved with screws in position No.5P/No.5D and close to the fracture site due to lower elastic strain value. Secured screws close to the fracture site reduced the translation and rotation of bone segments. The elastic strain increased when the distance of the first secured screw position from the fracture site increased, while increase in fracture gap width produced lower elastic strain. For 10-, 20-, and 30-mm gaps, elastic strain was minimized because the screws secured close to the fracture site increased stability.

B-LCP with screw positions No.4P/No.4D and/or No.5P/No.5D with an adjacent empty screw produced low elastic strain and bone stress, while EQV stress on implants increased to high values (441.2-566.1 MPa), leading to higher risk of implant breakage due to cyclic loads. Consequently, secured screws close to the fracture site should comprise at least three contiguous screws without an empty screw hole.

The CB-LCP without a secured screw close to the fracture site (positions No.4P/No.4D and No.5P/No.5D) produced low EQV stress and achieved low elastic strain and bone stress. High EQV stress resulted from secured screws close to the epiphysis regions. Fixation of screws close to the epiphysis regions should be avoided. Therefore, for mid-shaft fracture stabilized by CB-LCP, sufficient implant length should be able to secure screws with no less than 3 screws above and below the fracture for each segment.

Table 4 shows that the configuration with 8 screws gave better bone stress results than using other numbers of screws. Therefore, configurations having 8 screws on B-LCP and CB-LCP were sufficient and appropriate.

Only screw configurations with an identical number of screws and positions in both proximal and distal segments were included in this study. Cases of proximal and distal segments having different screw positions and numbers were excluded because too many FE analyses were required. Length of implant was also considered only for 12 holes due to the length of the femur obtained from the volunteer. Shorter lengths of implants than 12 holes were not considered due to the need to control geometries, while the number of elements of B-LCP/CB-LCP was identical in all simulated cases. The femur used in this analysis was acquired from a Thai subject and the radius of curvature varied from a Caucasian sample (Thiesen et al., 2018; Chantarapanich et al., 2008). As a result, biomechanical performances of bone-implant constructs may differ among diverse populations. In addition, this study focused on a transverse fracture at mid-shaft, while other fracture patterns were not assessed. It also carried out the B-LCB/CB-LCB in femur; other major long bones such as the tibia, humorous and radius require further investigation.

5. CONCLUSION

This study determined the optimal configuration and number of screws for B-LCP and CB-LCP to stabilize femoral shaft fractures. For B-LCP, screw position close to the fracture without adjacent screws should be avoided since it could produce high implant stress. Screw fixation close to fracture was suggested when CB-LCP is used due to lower exhibited stress. Better fracture stability can be achieved by screw fixation close to the fracture site, which produced lower elastic strain at the fracture site. Four screws for each segment presented better bone stress results than using other numbers of screws. Overall, there should be four screws on each fragment for both B-LCP and CB-LCP.

ACKNOWLEDGMENT

This research was funded by Kasetsart University through the Graduate School Fellowship Program.

REFERENCES

Amornmoragot, T. (2019). Comparison of comminuted femoral shaft fracture treatment between locking compression plate and conventional dynamic compression plate methods: A historical control an interventional study. *Thai Journal of Orthopaedic Surgery*, 43(1–2), 18–25.

Apivatthakakul, T., Phornphutkul, C., Bunmaprasert, T., Sananpanich, K., and Dell'Oca, A. F. (2012). Percutaneous cerclage wiring and minimally invasive plate osteosynthesis (MIPO): A percutaneous reduction technique in the treatment of Vancouver type B1 periprosthetic femoral shaft fractures. *Archives of Orthopaedic and Trauma Surgery*, 132(6), 813–822.

Bäcker, H. C., Heyland, M., Wu, C. H., Perka, C., Stöckle, U., and Braun, K. F. (2022). Breakage of intramedullary femoral nailing or femoral plating: How to prevent implant failure. *European Journal of Medical Research*, 27, 7.

Behrens, B.-A., Nolte, I., Wefstaedt, P., Stukenborg-Colsman, C., and Bouguecha, A. (2009). Numerical investigations on the strain-adaptive bone remodeling in the periprosthetic femur: Influence of the boundary conditions. *BioMedical Engineering OnLine*, 8, 7.

Bucholz, R. W., Court-Brown, C. M., Heckman, J. D., and Tornetta, P. (2010). *Rockwood and Green's Fractures in Adults,* 7th, Philadelphia: Wolters Kluwer Health, Lippincott Williams & Wilkins, pp. 162–190.

Chaitat, S., Chantarapanich, N., and Wanchat, S. (2022). Effects of the 3DP process parameters on mechanical properties of polylactic acid part used for medical purposes. *Rapid Prototyping Journal*, 28(1), 143–160.

Chantarapanich, N., and Riansuwan, K. (2022). Biomechanical performance of short and long cephalomedullary nail constructs for stabilizing different levels of subtrochanteric fracture. *Injury*, 53(2), 323–333.

Chantarapanich, N., Siripanya, A., Sucharitpwatskul, S., and Wanchat, S. (2017). Validation of finite element model used to analyze sheet metal punching process in automotive part manufacturing. *IOP Conference Series: Materials Science and Engineering,* 201, 012017.

Chantarapanich, N., Sitthiseripratip, K., Mahaisavariya, B., and Siribodhi, P. (2016). Biomechanical performance of retrograde nail for supracondylar fractures stabilization. *Medical and Biological Engineering and Computing*, 54(6), 939–952.

Chantarapanich, N., Sitthiseripratip, K., Mahaisavariya, B., Wongcumchang, M., and Siribodhi, P. (2008). 3D geometrical assessment of femoral curvature: A reverse engineering technique. *Journal of the Medical Association of Thailand*, 91(9), 1377–1381.

Chen, G., Schmutz, B., Wullschleger, M., Pearcy, M. J., and Schuetz, M. A. (2010). Computational investigations of mechanical failures of internal plate fixation. *Proceedings of the Institution of Mechanical Engineers*, 224(1), 119–126.

Dang, K. H., Armstrong, C. A., Karia, R. A., and Zelle, B. A. (2019). Outcomes of distal femur fractures treated with the synthes 4.5 mm VA-LCP curved condylar plate. *International Orthopaedics,* 43(7), 1709–1714.

Fedorov, A., Beichel, R., Kalpathy-Cramer, J., Finet, J., Fillion-Robin, J.-C., Pujol, S., Bauer, C., Jennings, D., Fennessy, F., Sonka, M., Buatti, J., Aylward, S., Miller, J. V., Pieper, S., and Kikinis, R. (2012). 3D slicer as an image computing platform for the quantitative imaging network. *Magnetic Resonance Imaging*, 30(9), 1323–1341.

Jitprapaikulsarn, S., Chantarapanich, N., Gromprasit, A., Mahaisavariya, C., and Patamamongkonchai, C. (2021). Single lag screw and reverse distal femur locking compression plate for concurrent cervicotrochanteric and shaft fractures of the femur: Biomechanical study validated with a clinical series. *European Journal of Orthopaedic Surgery and Traumatology*, 31(6), 1179–1192.

Johnson, E. E., and Urist, M. R. (2000). Human bone morphogenetic protein allografting for reconstruction of femoral nonunion. *Clinical Orthopaedics and Related Research*, 371, 61–74.

Kim, D.-S., Kim, Y.-M., Choi, E.-S., Shon, H.-C., Park, K.-J., Cho, B.-K., Park, J.-K., Lee, H.-C., and Hong, K.-H. (2012). Repeated metal breakage in a femoral shaft fracture with lateral bowing: A case report. *Journal of the Korean Fracture Society*, 25(2), 136–141.

Koval, K. J., Sala, D. A., Kummer, F. J., and Zuckerman, J. D. (1998). Postoperative weight-bearing after a fracture of the femoral neck or an intertrochanteric fracture. *Journal of Bone and Joint Surgery*, 80(3), 352–356.

Krone, R., and Schuster, P. (2006). An investigation on the importance of material anisotropy in finite-element modeling of the human femur. *SAE Technical Papers*, 2006-01-0064.

Lee, C.-H., Shih, K.-S., Hsu, C.-C., and Cho, T. (2014). Simulation-based particle swarm optimization and mechanical validation of screw position and number for the fixation stability of a femoral locking compression plate. *Medical Engineering and Physics*, 36(1), 57–64.

Lv, H., Chang, W., Yuwen, P., Yang, N., Yan, X., and Zhang, Y. (2017). Are there too many screw holes in plates for fracture fixation? *BMC Surgery*, 17, 46.

Marcomini, J. B., Baptista, C. A. R. P., Pascon, J. P., Teixeira, R. L., and Reis, E. P. (2014). Investigation of a fatigue failure in a stainless steel femoral plate. *Journal of the Mechanical Behavior of Biomedical Materials*, 38, 52–58.

Marsell, R., and Einhorn, T. A. (2011). The biology of fracture healing. *Injury*, 42(6), 551–555.

Meinberg, E. G., Agel, J., Roberts, C. S., Karam, M. D., and Kellam, J. F. (2018). Fracture and dislocation classification compendium–2018. *Journal of Orthopaedic Trauma*, 32(Suppl 1), S1–S10.

Padron, A. A., Owen, J. R., Wayne, J. S., Aktay, S. A., and Barnes, R. F. (2017). *In vitro* biomechanical testing of the 3.5 mm LCP in torsion: A comparison of unicortical locking to bicortical nonlocking screws placed nearest the fracture gap. *BMC Research Notes*, 10, 768.

Rostamian, R., Silani, M., Ziaei-Rad, S., Busse, B., Qwamizadeh, M., and Rabczuk T. (2022). A finite element study on femoral locking compression plate design using genetic optimization method. *Journal of the Mechanical Behavior of Biomedical Materials*, 131, 105202.

Sheng, W., Ji, A., Fang, R., He, G., and Chen, C. (2019). Finite element and design of experiment-derived optimization of screw configurations and a locking plate for internal fixation system. *Computational and Mathematical Methods in Medicine*, 2019, 5636528.

Sivarao, S., Leong, S. T., Yusof, Y., and Tan, C. F. (2015). An experimental and numerical investigation of tensile properties of stone wool fiber reinforced polymer composites. *Advanced Materials Letters*, 6(10), 888–894.

Speirs, A. D., Heller, M. O., Duda, G. N., and Taylor, W. R. (2007). Physiologically based boundary conditions in finite element modelling. *Journal of Biomechanics*, 40(10), 2318–2323.

Tank, J. C., Schneider, P. S., Davis, E., Galpin, M., Prasarn, M. L., Choo, A. M., Munz, J. W., Achor, T. S., Kellam, J. F., and Gary, J. L. (2016). Early mechanical failures of the synthes variable angle locking distal femur plate. *Journal of Orthopaedic Trauma*, 30(1), e7–e11.

Taylor, W. R., Roland, E., Ploeg, H., Hertig, D., Klabunde, R., Warner, M. D., Hobatho, M. C., Rakotomanana, L., and Clift, S. E. (2002). Determination of orthotropic bone elastic constants using FEA and modal analysis. *Journal of Biomechanics*, 35(6), 767–773.

Thiesen, D. M., Prange, F., Berger-Groch, J., Ntalos, D., Petersik, A., Hofstätter, B., Rueger, J. M., Klatte, T. O., and Hartel, M. J. (2018). Femoral antecurvation – A 3D CT analysis of 1232 adult femurs. *PLOS One*, 13(10), e0204961.

Wagner, M. (2003). General principles for the clinical use of the LCP. *Injury*, 34(Suppl 2), B31–B42.

Wittkowske, C., Raith, S., Eder, M., Volf, A., Kirschke, J. S., König, B., Ihle, C., Machens, H.-G., Döbele, S., and Kovacs, L. (2017). Computer assisted evaluation of plate osteosynthesis of diaphyseal femur fracture considering interfragmentary movement: A finite element study. *Biomedizinische Technik,* 62(3), 245–255.

SUPPLEMENTARY DATA

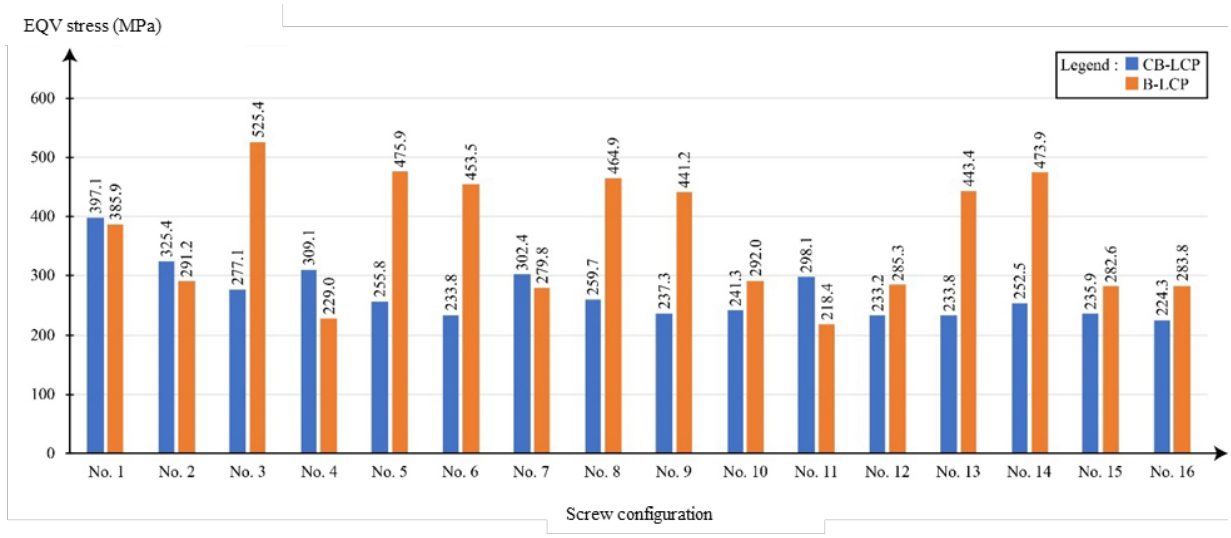

Figure S1. Maximum implant stress magnitude on B-LCP and CB-LCP for fracture gap width 10 mm

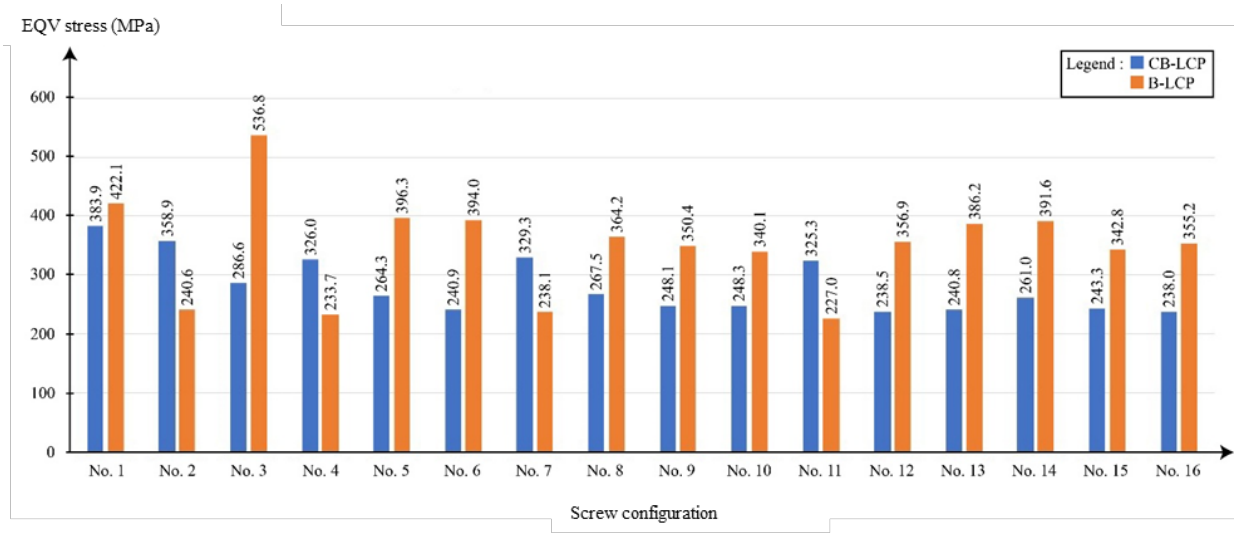

Figure S2. Maximum implant stress magnitude on B-LCP and CB-LCP for fracture gap width 20 mm

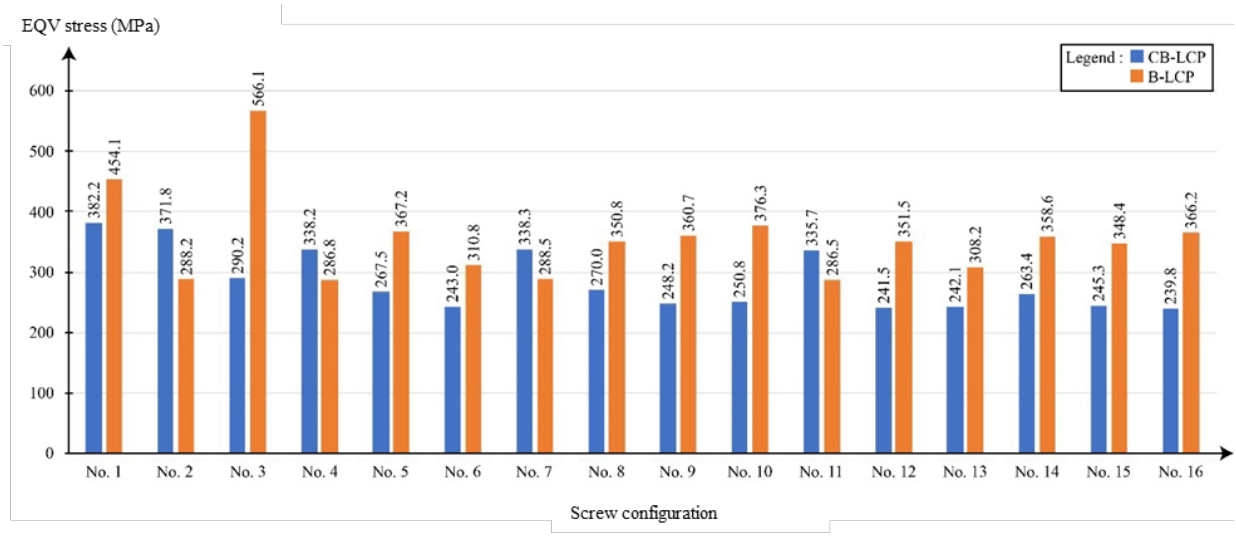

Figure S3. Maximum implant stress magnitude on B-LCP and CB-LCP for fracture gap width 30 mm

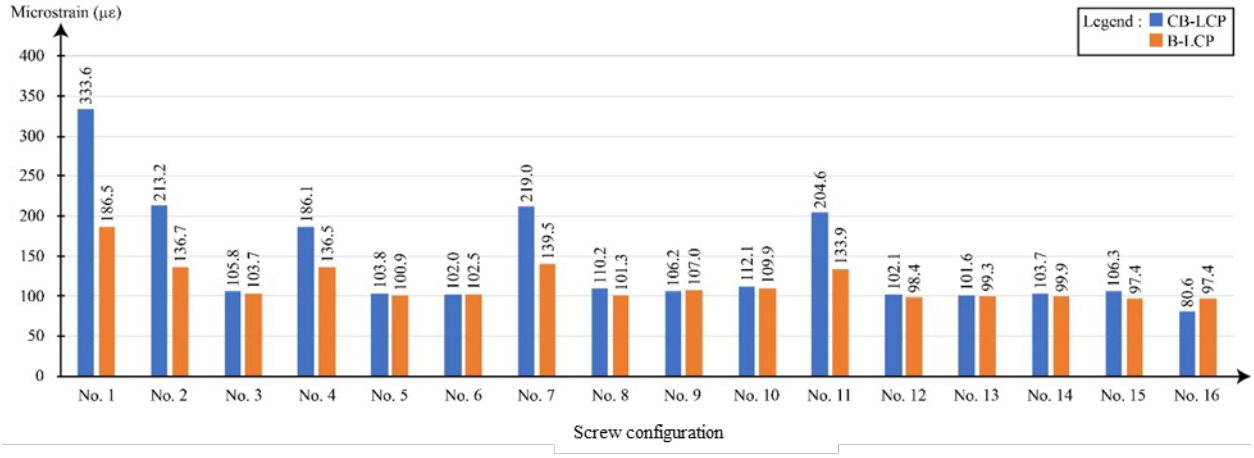

Figure S4. Elastic strain at fracture site stabilized by B-LCP and CB-LCP for fracture gap width 10 mm

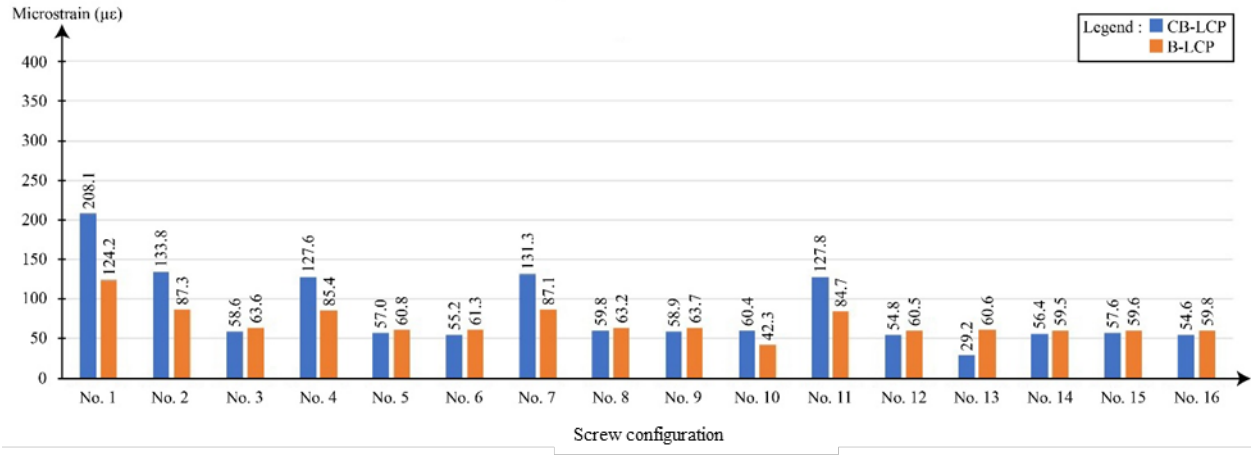

Figure S5. Elastic strain at fracture site stabilized by B-LCP and CB-LCP for fracture gap width 20 mm

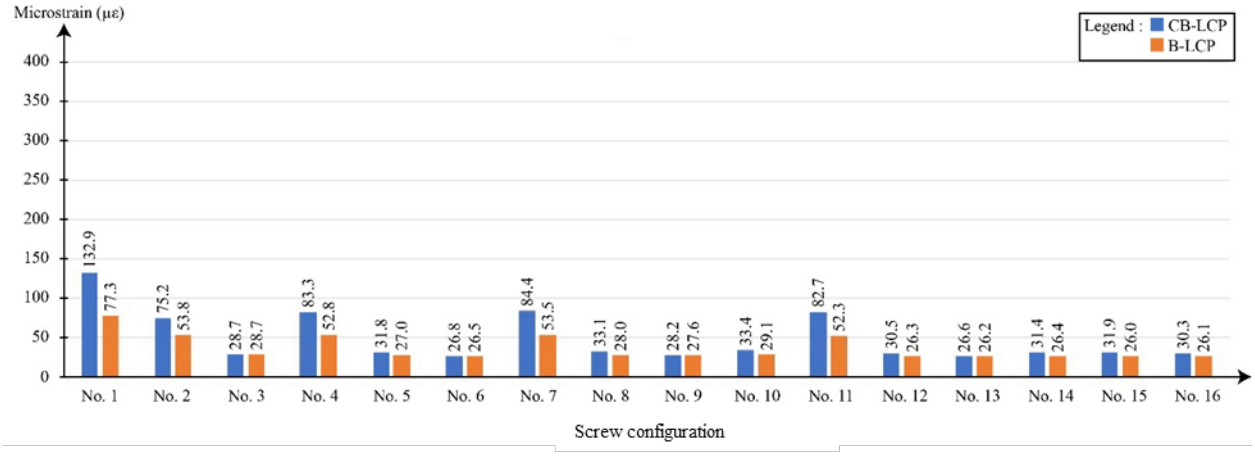

Figure S6. Elastic strain at fracture site stabilized by B-LCP and CB-LCP for fracture gap width 30 mm

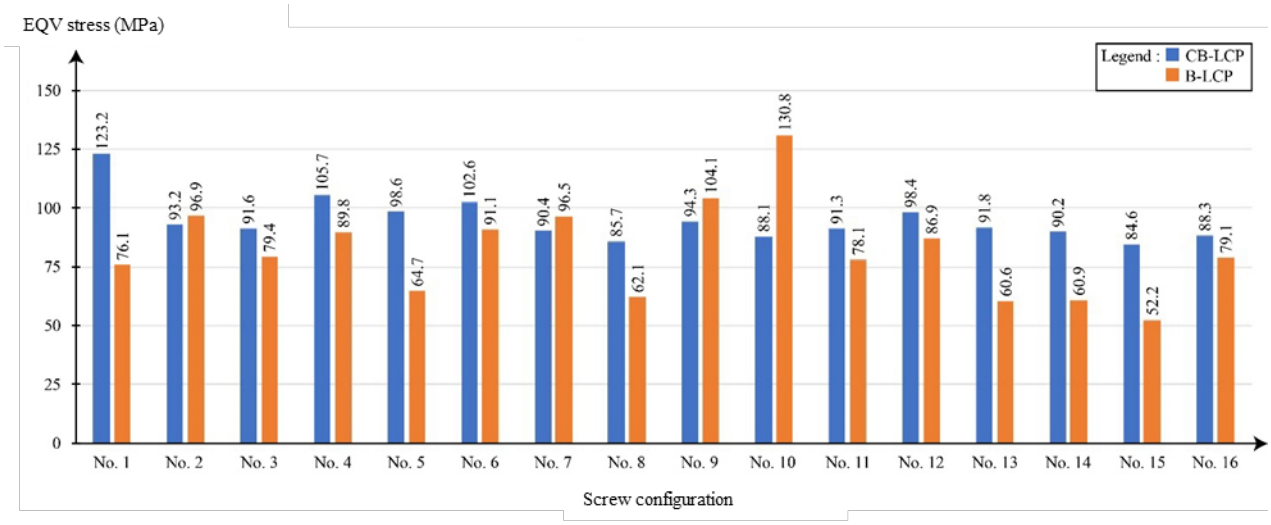

Figure S7. Bone stress magnitude when retained with B-LCP and CB-LCP for fracture gap width 10 mm

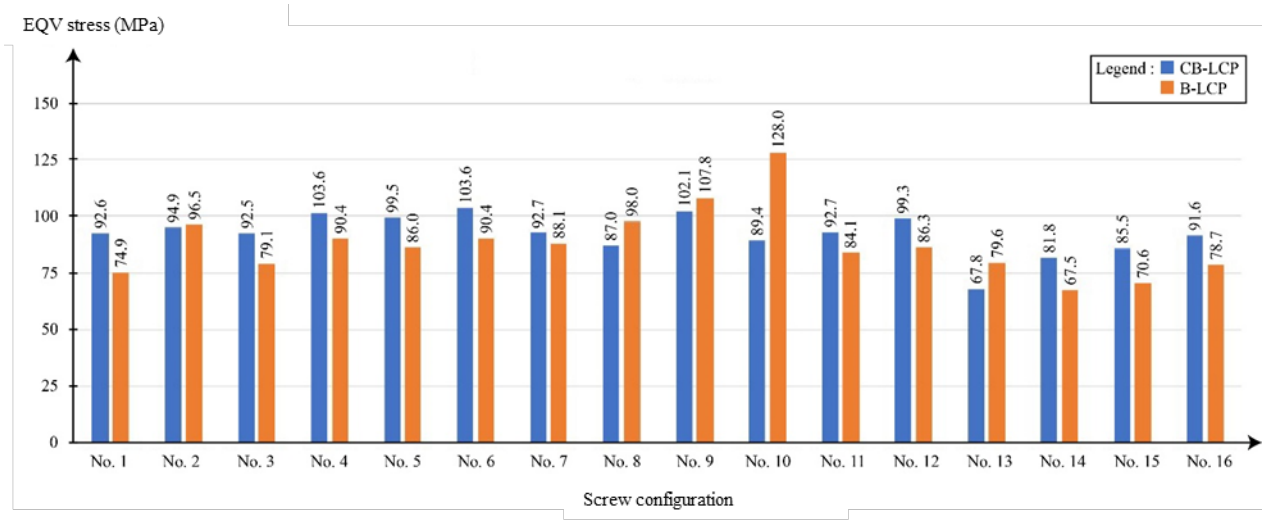

Figure S8. Bone stress magnitude when retained with B-LCP and CB-LCP for fracture gap width 20 mm

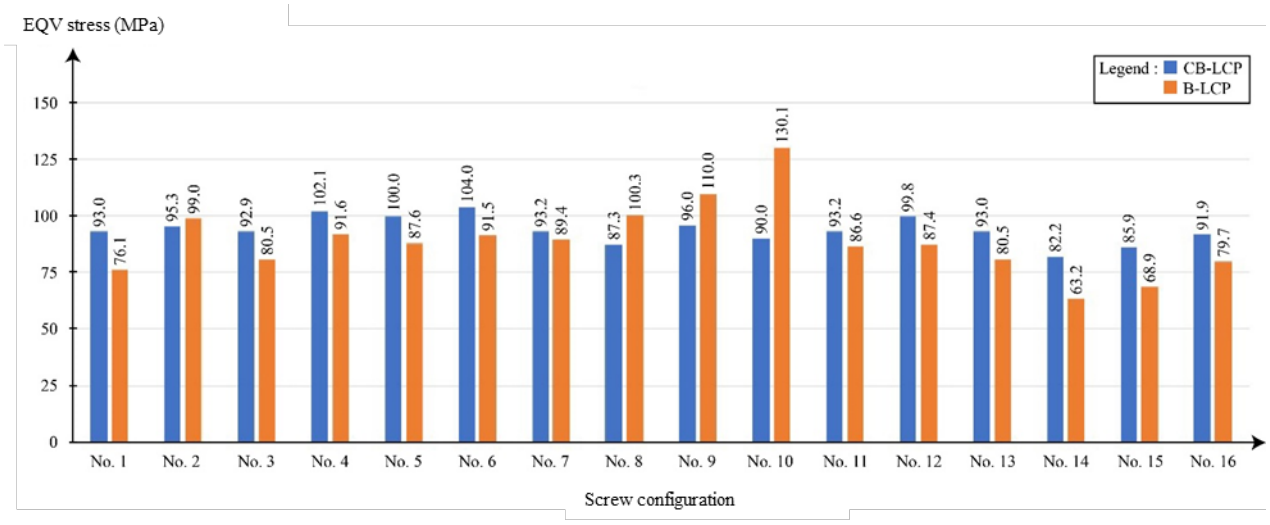

Figure S9. Bone stress magnitude when retained with B-LCP and CB-LCP for fracture gap width 30 mm